Supplementary Information

Single-Atom Tailored Atomically-Precise Nanoclusters for Enhanced Electrochemical CO_2 Reduction Activity

Henan Key Laboratory of Crystalline Molecular Functional Materials, Green Catalysis Center, and College of Chemistry, Zhengzhou University, Zhengzhou 450001, China.

Yi-Man Wang, Fang-Qin Yan, Qian-You Wang, Chen-Xia Du, Shan Wang* & Shuang-Quan Zang*

E-mail: zangsqzg@zzu.edu.cn; shanwang@zzu.edu.cn

DOI: XXXXX

Characterization: Single-crystal X-ray diffraction (SCXRD) was performed on a Rigaku XtaLAB Pro diffractometer using Cu Kα radiation (λ = 1.54184 Å). Powder X-ray diffraction (PXRD) were collected on a Riguku D / Max-2500PC X-ray diffractometer with Cu sealed tub (λ = 1.54178 Å). Morphology of all samples were carried out using Zeiss Sigma 500 on a scanning electron microscopy (SEM) measurement. The Poly-(Au_8-DCP@M), Poly-(Au_8-DCP), Poly-Au_8 and Poly-DCP@Fe were prepared by employing the CH660E B14145 electrochemical workstation. Fourier transform infrared (FT-IR) spectra were recorded on a Bruker ALPHA II FT-IR spectrometer. ^{1}H nuclear magnetic resonance (NMR) spectra were recorded on a Bruker DRX spectrometer operating at 400 MHz. Transmission electron microscopy (TEM) images were obtained in FEI TalosF200S. Aberration-corrected HAADF-STEM (AC HAADF-STEM) images were obtained in FEI Titan cubed Themis G2 300 STEM with aspherical aberration corrector. The produced gas was monitored by Agilent GC7820 Gas Chromatograph (N_2 as gas carrier, and the columns of GC are Porapak Q and MolSieve 5A). The CO_2RR reaction pathways of as-prepared catalysts were detected via in situ ATR-FTIR spectrometer (BRUKER INVENIO S).

Cyclic voltammetry (CV) curves in electrochemical double-layer capacitance (Cdl) determination were measured in a potential window nearly without the faradaic process at different scan rates of 10, 20, 30, 40 and 50 mV s^{-1}. The plot of current density at set potential against scan rate has a linear relationship and its slope is the Cdl.

TEM sample preparation: The obtained Poly-(Au_8-DCP@Fe) was dispersed in 1 mL ethanol by ultrasound to form a suspension, which was then dropped on carbon film. The carbon film was dried under air within a few seconds and further used for TEM characterizations.

***In-situ* ATR-FTIR experiments:** *In-situ* ATR-FTIR tests were implemented by Bruker INVENIO S FT-IR spectrophotometer equipped with a liquid N_2-cooled MCT detector. To enhance the in-situ ATR-FTIR signal and electronic conduction, the ultra-thin gold foil was chemically deposited on the silicon. The working electrode for the in-situ ATR-FTIR test was prepared by dropping the electrocatalyst on Au membrane.

***In-situ* CO-DRIFTS experiments:** *In-situ* CO-DRIFTS was performed on a Bruker INVENIO S FT-IR spectrophotometer equipped with an MCT narrow-band detector and a modified in situ reaction cell with a drier device. The detailed pretreatment and test conditions are given as follows. Firstly, the sample was carefully put into the support sheet of reaction cell, and a pure Ar stream (50 mL min^{-1}) was introduced for 20 min to remove the gaseous impurities in the cell. Subsequently, the sample was pre-reduced in a 5 % H_2/Ar flow (50 mL min^{-1}) at 300 °C for 2 h, followed cooled 1.0 h to 25 °C in a pure Ar stream, and the background spectrum was collected in this process. Finally, the DRIFTS spectra was collected after introducing the 2 % CO/N_2 (50 mL min^{-1}) to the cell for 1.0 h.

Supplementary Tab. 1. Crystal data and structure refinements.

Complex	Au_8
CCDC	2290525
Empirical formula	$C_{148}H_{128}Au_8N_2P_8$
Formula weight	3758.05
Temperature/K	200(10)
Crystal system	monoclinic
Space group	*C*2/c
a (Å)	40.48288(17)
b (Å)	17.18787(7)
c (Å)	24.82685(10)
α (°)	90
β (°)	103.6391(4)
γ (°)	90
Volume (Å^3)	16787.73(12)
Z	4
ρ/Mg cm^{-3}	1.492
μ/mm^{-1}	13.858
F(000)	7153.0
Crystal size/mm	0.03 ×0.02 × 0.02
Radiation	CuKα (λ = 1.54184)
2Θ range for data collection/°	5.612 to 147.518
Index ranges	$-49 \le h \le 48$, $-18 \le k \le 21$, $-28 \le l \le 30$
Reflections collected	54141
Independent reflections	16597 [R_{int} = 0.0329, R_{sigma} = 0.0324]
Data/restraints/parameters	16597/0/748
GOF on F^2	1.069
Final R indexes [I >= 2σ (I)]	R_1 = 0.0239, wR_2 = 0.0612
Final R indexes [all data]	R_1 = 0.0270, wR_2 = 0.0624
Largest diff. peak/hole/e Å^{-3}	0.81 / -0.73

$R_1 = \sum||F_o|-|F_c||/\sum|F_o|$. $wR_2 = [\sum w(F_o^2 - F_c^2)^2/\sum w(F_o^2)^2]^{1/2}$

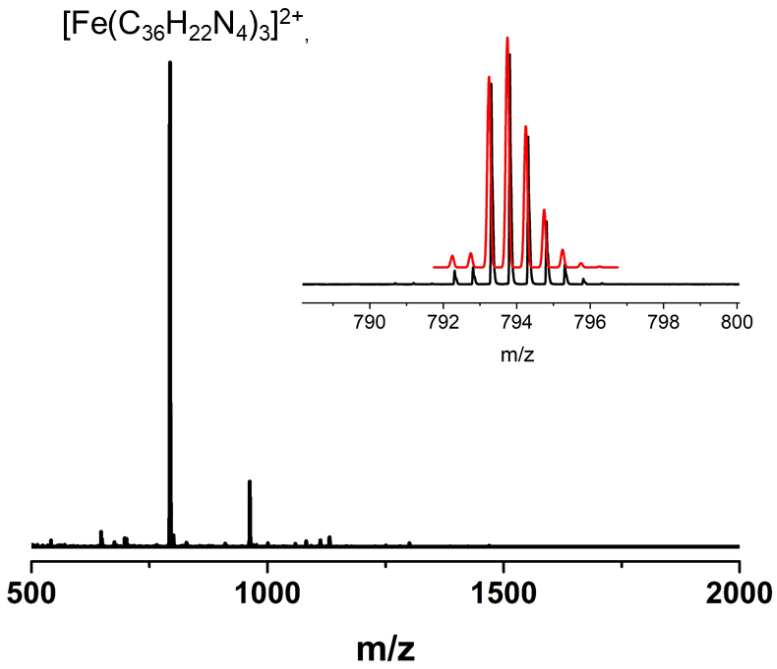

Supplementary Figure 1. Positive mode ESI-MS of the DCP@Fe ($[Fe(C_{36}H_{22}N_4)_3]^{2+}$, m/z = 793.75).

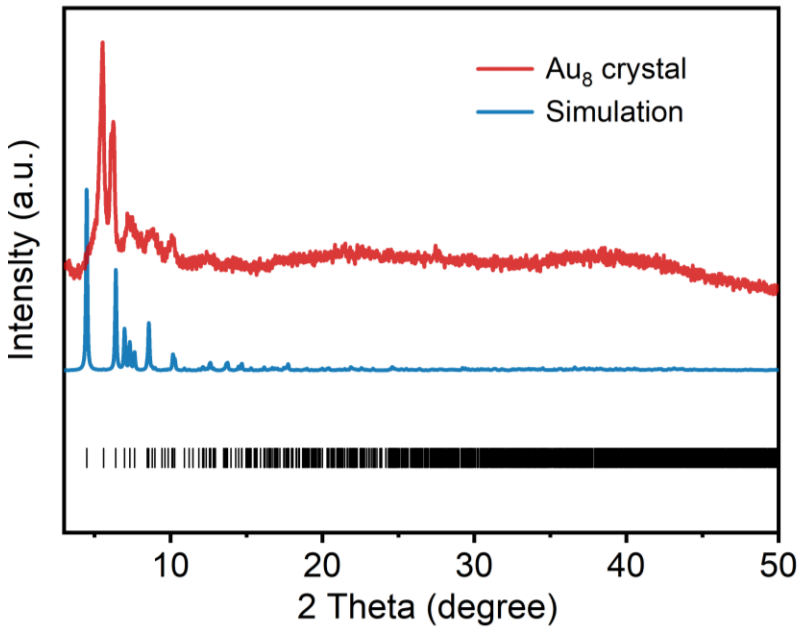

Supplementary Figure 2. PXRD patterns of simulated Au_8 and single crystal of Au_8.

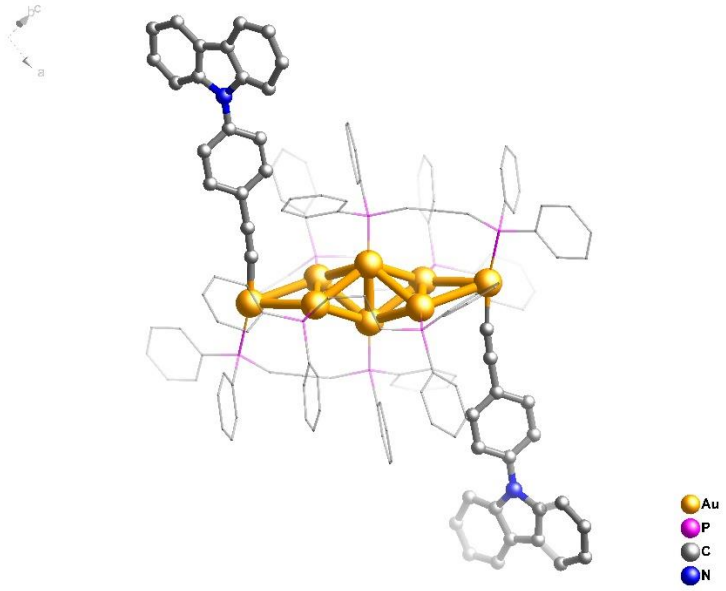

Supplementary Figure 3. Views of crystal structures of Au_8 crystal. All H-atoms have been omitted for clarity (orange = Au, purple = P, gray = C, blue = N).

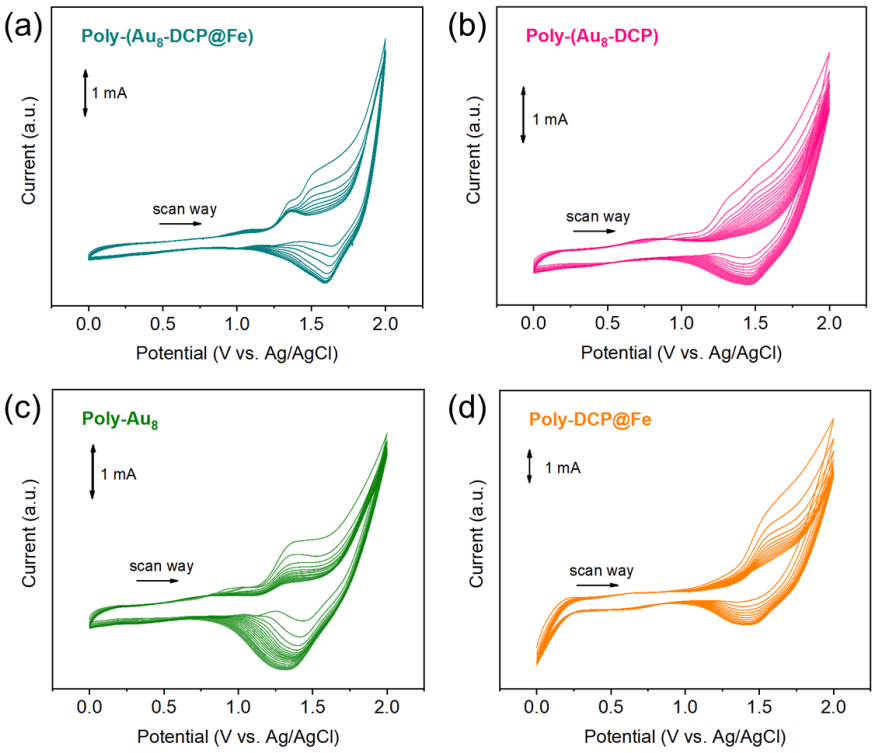

Supplementary Figure 4. CV profiles of the electropolymerization process recorded on CP electrode (area = 1 × 1 cm^{-2}).

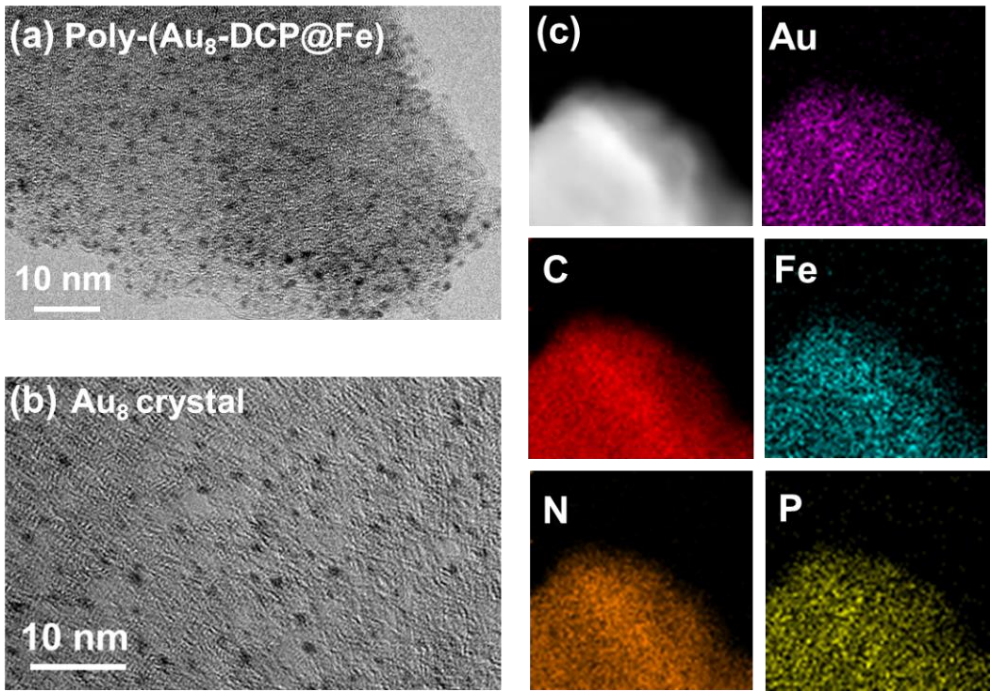

Supplementary Figure 5. TEM images of (a) Poly-(Au_8-DCP@Fe) and (b) Au_8 crystal, (c) EDS mapping of Poly-(Au_8-DCP@Fe).

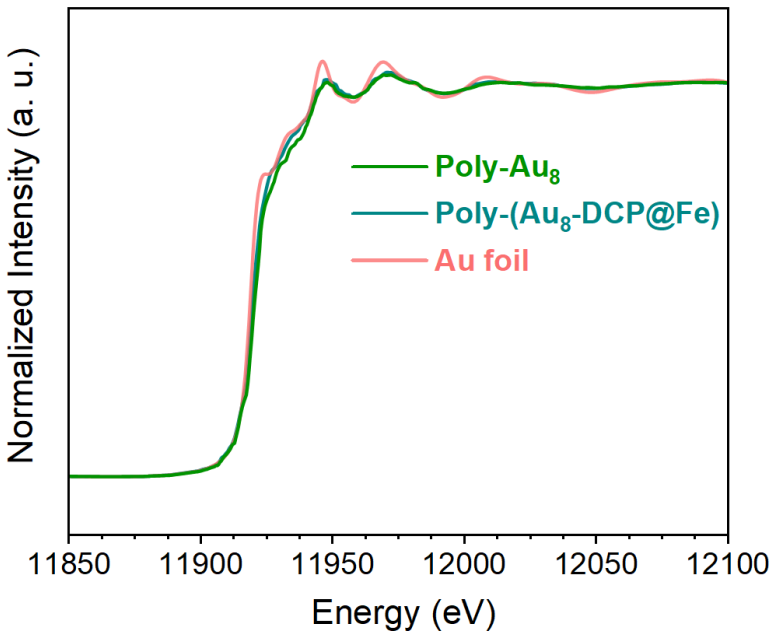

Supplementary Figure 6. The Au L_3-edge XANES of Au foil, Poly-Au_8 and Poly-(Au_8-DCP@Fe).

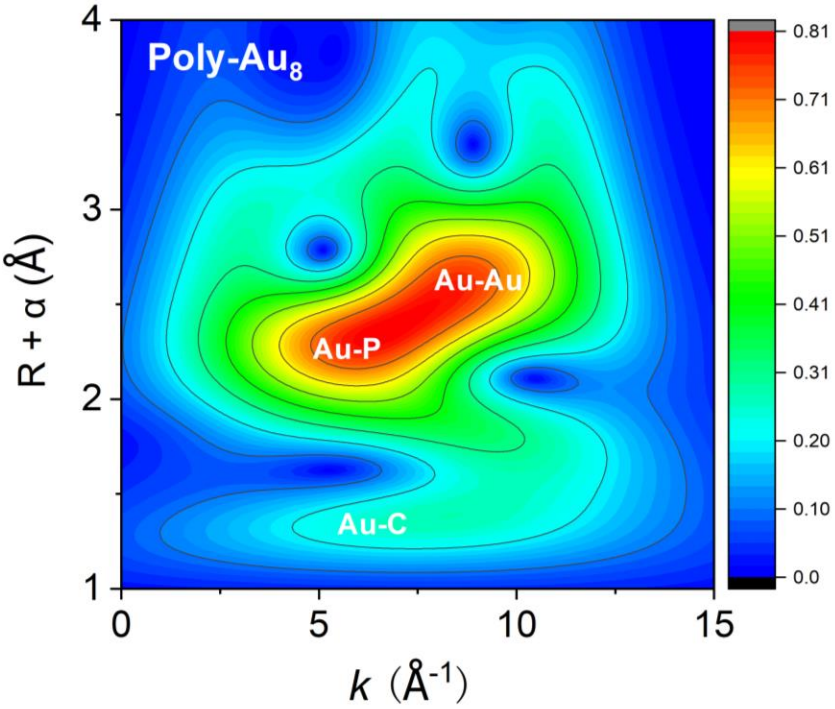

Supplementary Figure 7. Wavelet transform of Au L_3-edge EXAFS for Poly-Au_8.

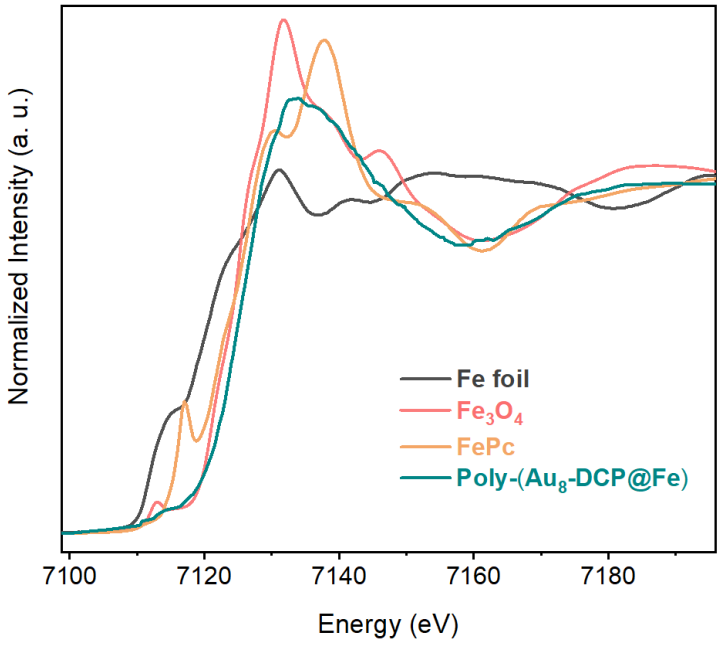

Supplementary Figure 8. The Fe *K*-edge XANES of Fe foil, Fe_3O_4, FePc and Poly-(Au_8-DCP@Fe).

Supplementary Tab. 2. EXAFS fitting parameters at the Au L_3-edge and Fe K-edge for various samples（S_0^2=0.83）

	shell	CN	R(Å)	σ^2	ΔE_0	R factor
Fe foil	Fe-Fe1	8	2.47±0.01	0.0047	6.5±0.8	0.0033
	Fe-Fe2	6	2.85±0.01	0.0060		
Au foil	Au-Au	12	2.86±0.01	0.0081	4.8±0.3	0.0016
Poly-(Au_8-DCP@Fe)	Au-C	0.9±0.3	1.95±0.02	0.0042	-15	
	Au-P	0.7±0.3	2.41±0.04	0.0114	-15	0.0163
	Au-Au	10.2±0.8	2.86±0.01	0.0152	7.0±1.3	
	Fe-N	5.9±0.6	2.02±0.02	0.0103	0.6±3.0	0.0121

[a]*CN*: coordination numbers; [b]*R*: bond distance; [c]σ^2: Debye-Waller factors; [d] ΔE_0: the inner potential correction. *R* factor: goodness of fit.

The obtained XAFS data was processed in Athena (version 0.9.26) for background, pre-edge line and post-edge line calibrations. Then Fourier transformed fitting was carried out in Artemis (version 0.9.26). The k^2 weighting, k-range of 3 – ~11.5 $Å^{-1}$ and R range of 1 - 3 Å were used for the fitting of Au foil and Sample. The four parameters, coordination number, bond length, Debye-Waller factor and E_0 shift (CN, R, ΔE_0) were fitted without anyone was fixed, the σ^2 was set.

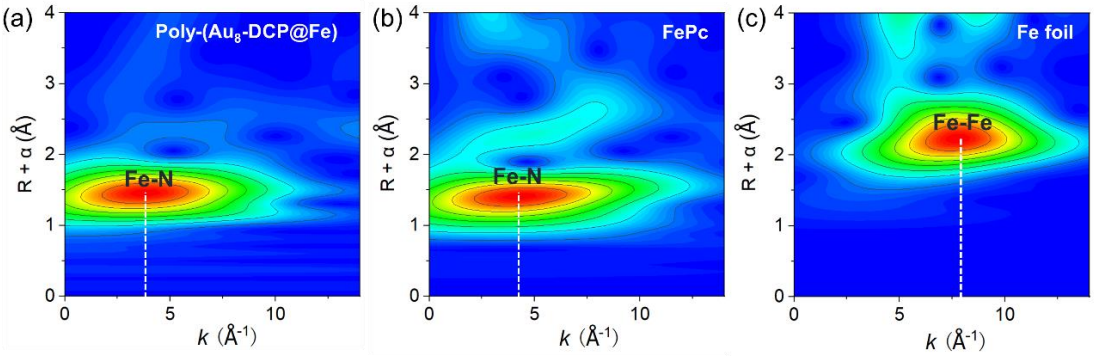

Supplementary Figure 9. Wavelet transform of Fe *K*-edge EXAFS for Poly-(Au_8-DCP@Fe), FePc and Fe foil.

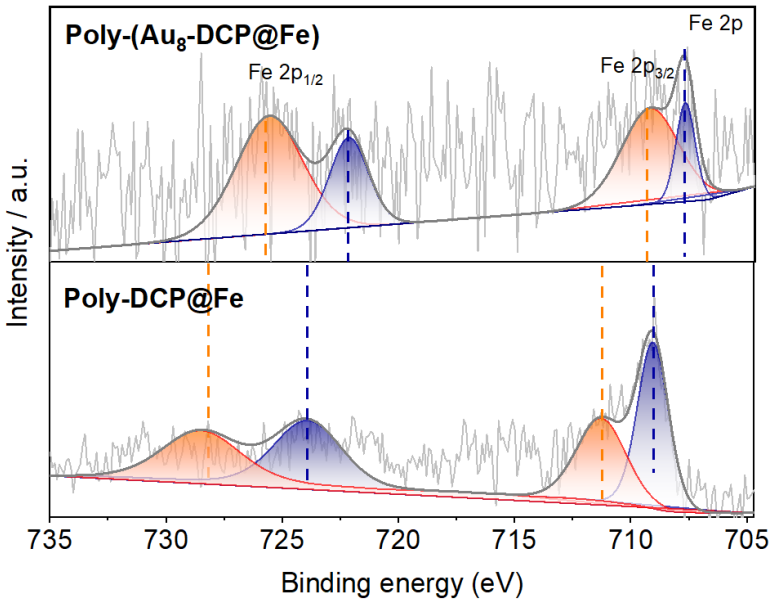

Supplementary Figure 10. XPS spectra of Fe 2p for (a) Poly-(Au$_8$-DCP@Fe) and (b) Poly-DCP@Fe.

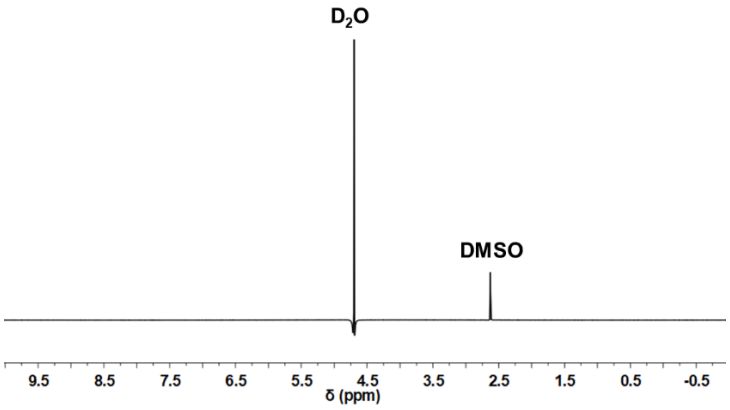

Supplementary Figure 11. ^{1}H NMR spectroscopy of the reaction mixture of Poly-(Au$_8$-DCP@Fe) after catalysis, DMSO was added as internal standard.

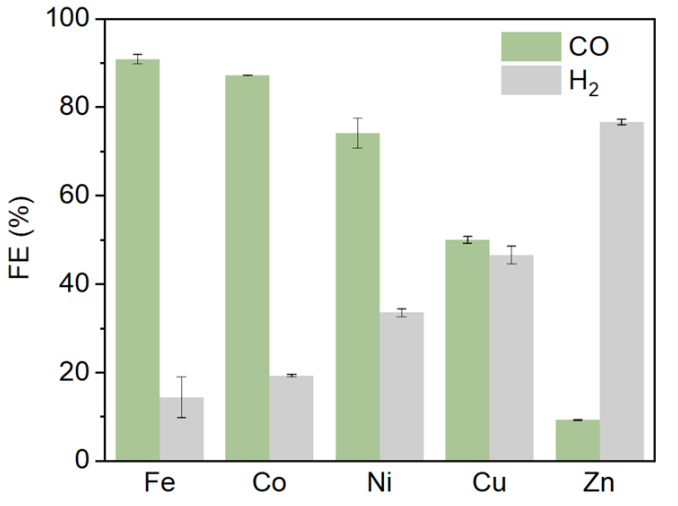

Supplementary Figure 12. Faradaic efficiencies of Poly-(Au$_8$-DCP@M) at different applied potentials in CO_2-saturated 0.5 M $KHCO_3$ aqueous solution.

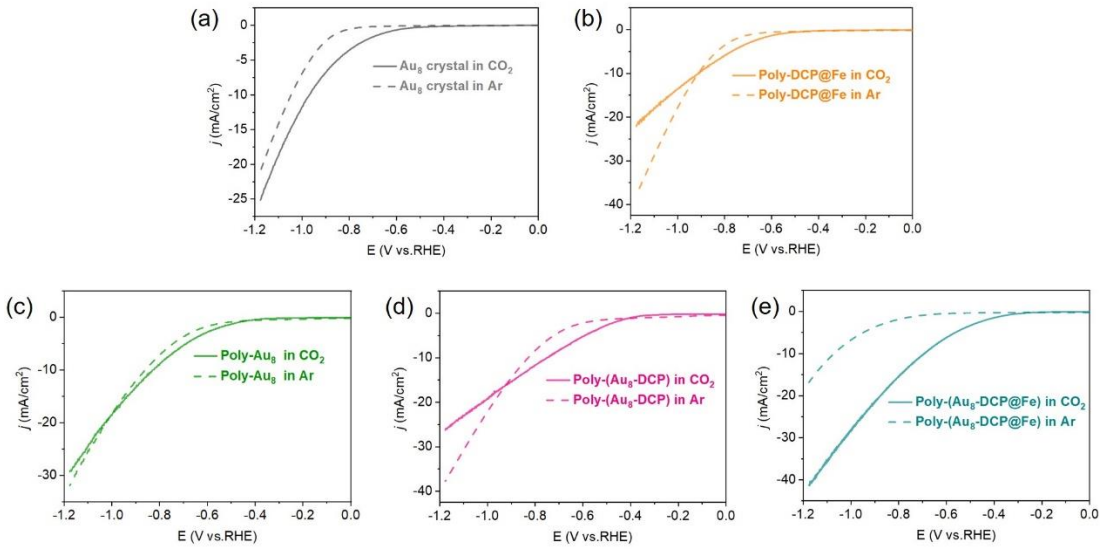

Supplementary Figure 13. LSV curves for (a) Au_8 crystal (b) Poly-DCP@Fe (c) Poly-Au_8 (d) Poly-(Au_8-DCP) and (e) Poly-(Au_8-DCP@Fe) in a CO_2-saturated and Ar-saturated $KHCO_3$ solution at the potential range of 0 to -1.17 V (vs RHE, scan rate of 50 mV/s).

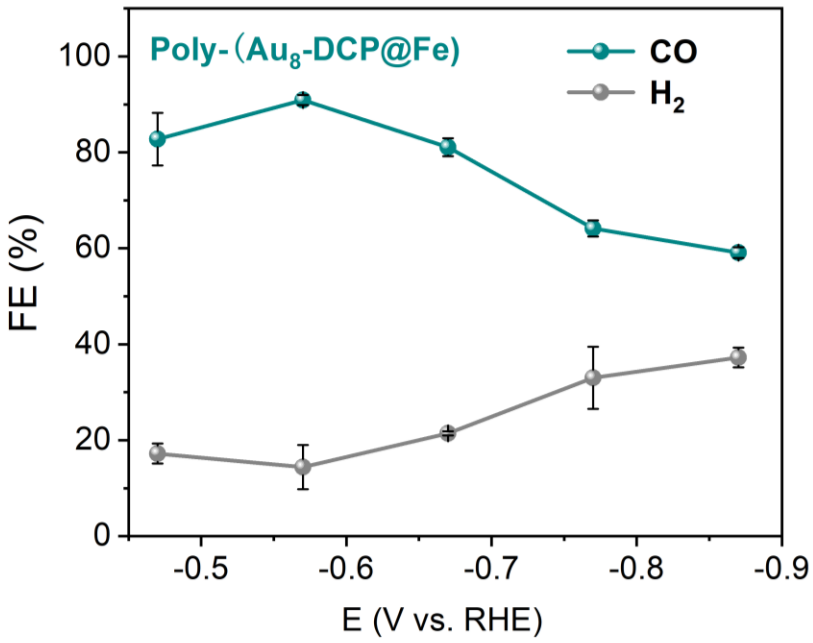

Supplementary Figure 14. Faradaic efficiencies of Poly-(Au_8-DCP@Fe) at different applied potentials in CO_2-saturated 0.5 M $KHCO_3$ aqueous solution.

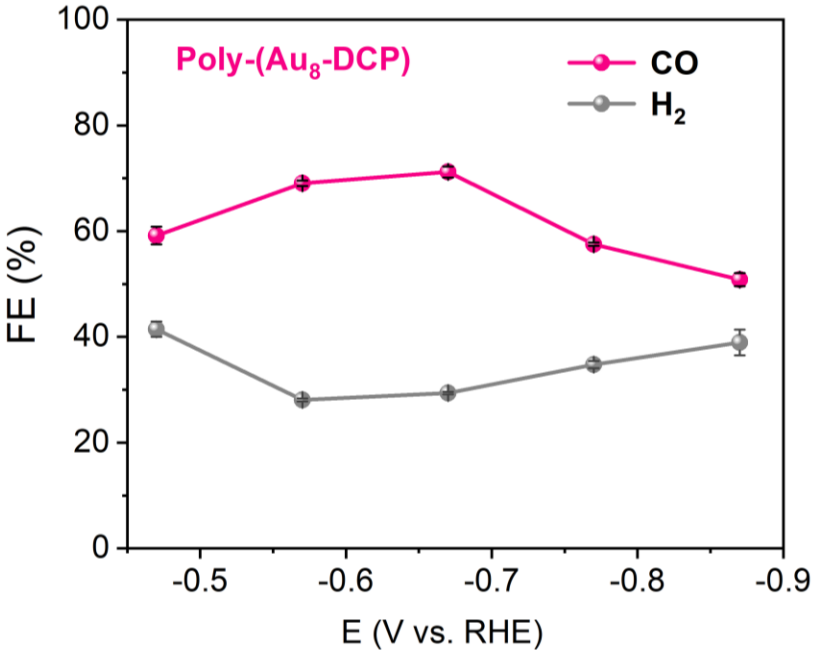

Supplementary Figure 15. Faradaic efficiencies of Poly-(Au_8-DCP) at different applied potentials in CO_2-saturated 0.5 M $KHCO_3$ aqueous solution.

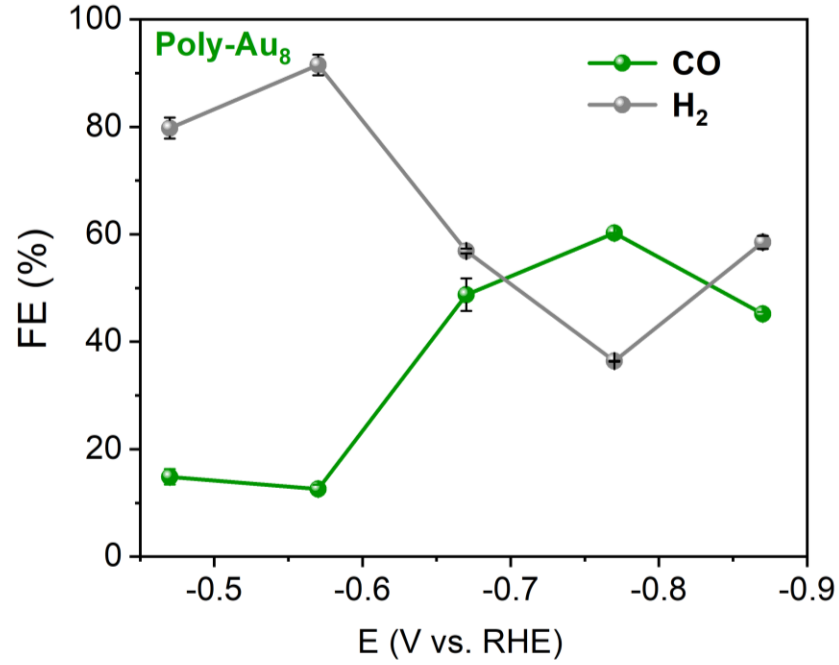

Supplementary Figure 16. Faradaic efficiencies of Poly-Au_8 at different applied potentials in CO_2-saturated 0.5 M $KHCO_3$ aqueous solution.

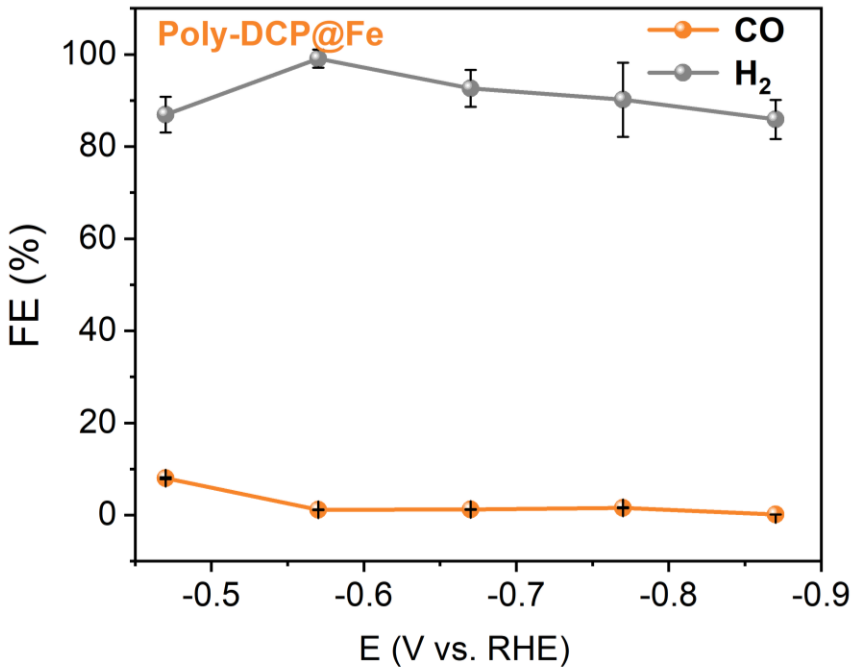

Supplementary Figure 17. Faradaic efficiencies of Poly-DCP@Fe at different applied potentials in CO_2-saturated 0.5 M $KHCO_3$ aqueous solution.

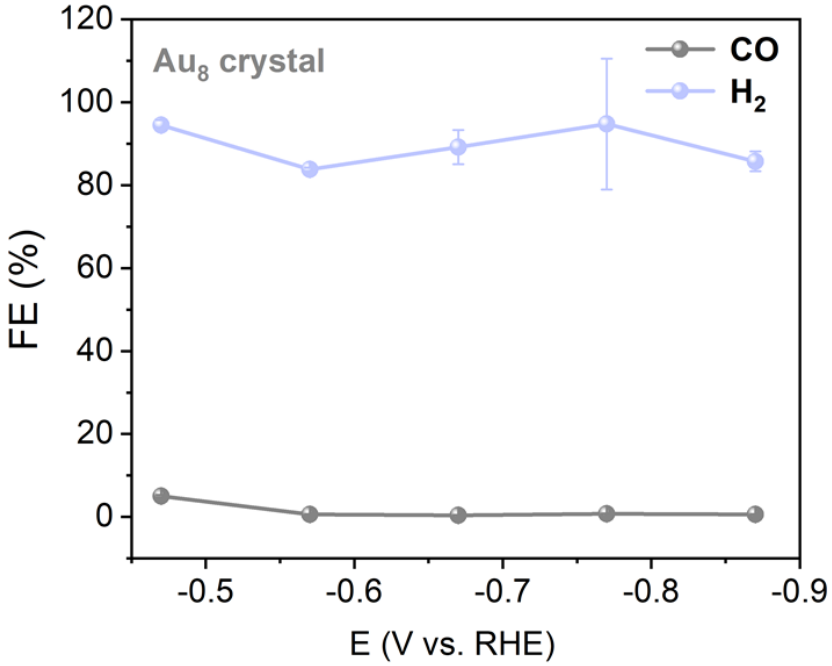

Supplementary Figure 18. Faradaic efficiencies of Au_8 crystal at different applied potentials in CO_2-saturated 0.5 M $KHCO_3$ aqueous solution.

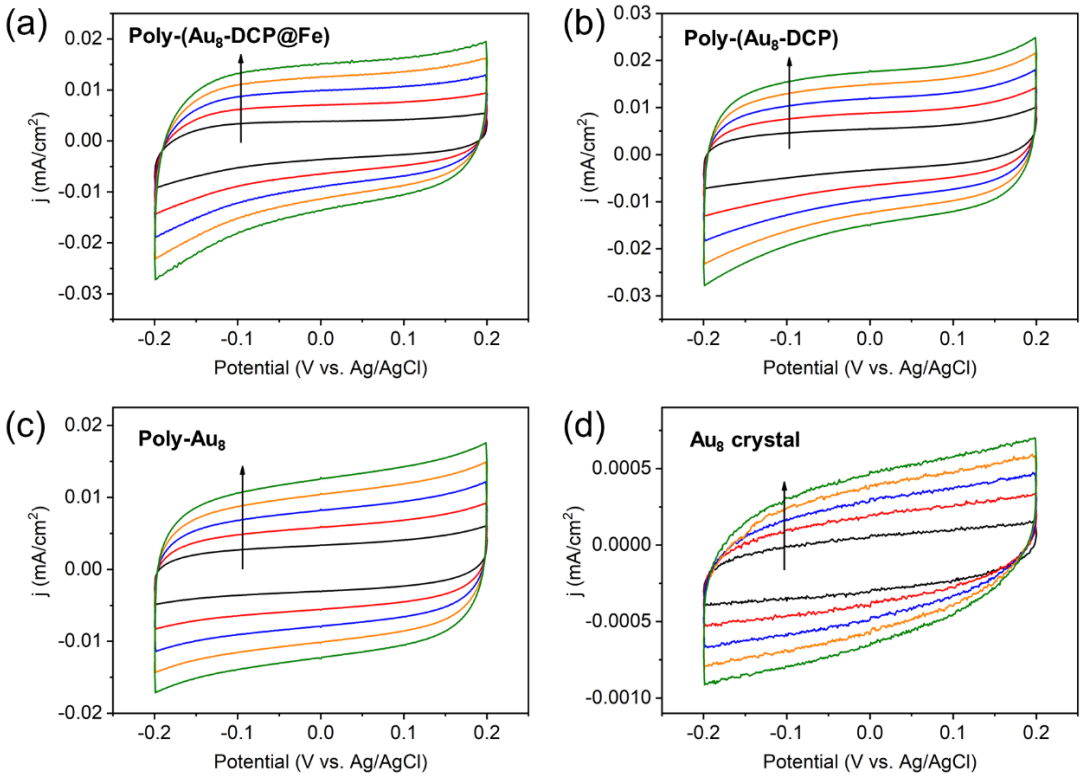

Supplementary Figure 19. CV curves of (a) Poly-(Au_8-DCP@Fe), (b) Poly-(Au_8-DCP), (c) Poly-Au_8, and (d) Au_8 crystal with various scan rates from 10 to 50 mV s^{-1}.

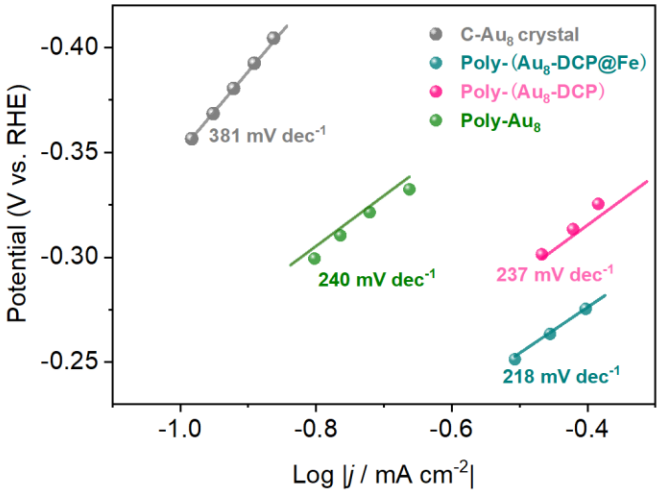

Supplementary Figure 20. Corresponding Tafel slopes for Poly-(Au_8-DCP@Fe), Poly-(Au_8-DCP), Poly-Au_8, Poly-DCP@Fe, and Au_8 crystal.

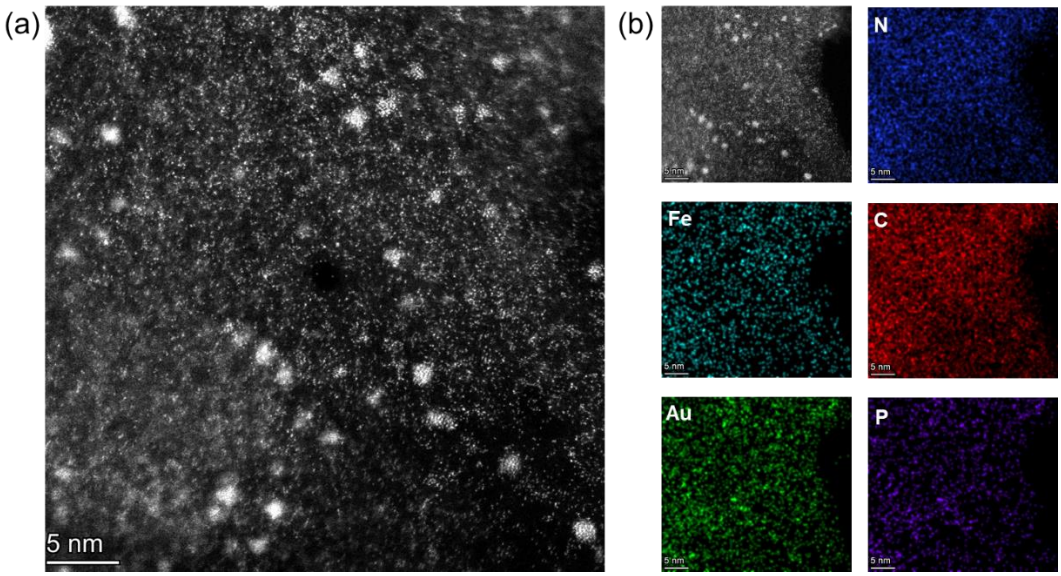

Supplementary Figure 21. (a) HAADF-STEM image and (b) Elemental mapping of Poly-(Au$_8$-DCP@Fe) after stability test.

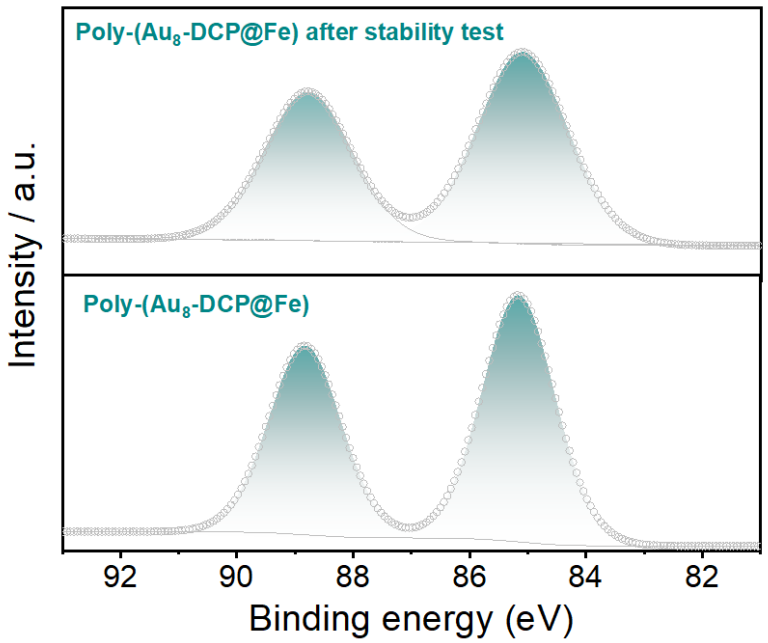

Supplementary Figure 22. XPS spectra of Au 4f in Poly-(Au$_8$-DCP@Fe) before and after stability test.

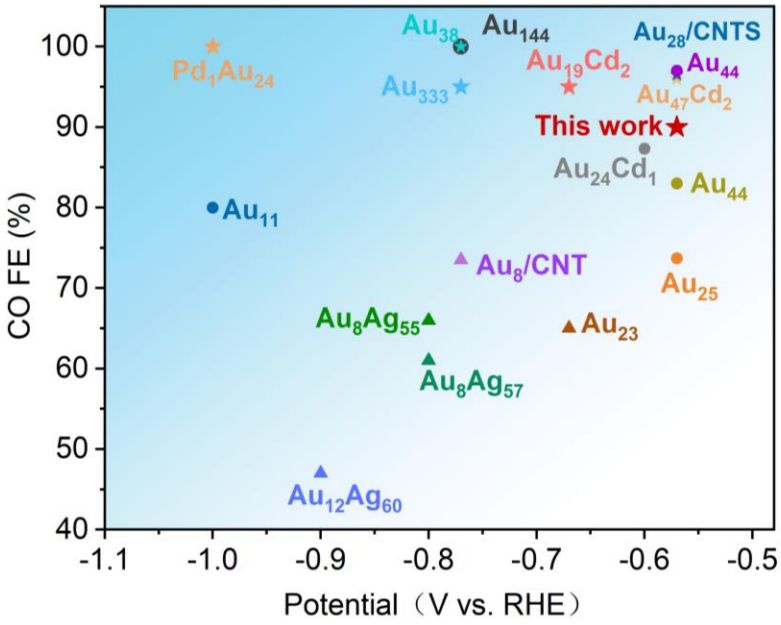

Supplementary Figure 23. CO FEs of Poly-(Au_8-DCP@Fe) compared with other representative Au NCs catalysts.

Supplementary Tab. 3 Comparison of CO_2RR performance of Poly-(Au_8@DCP@Fe) with other representative Au nanoclusters catalysts.

Cathode	electrolyte	Potential（V vs. RHE）	CO FE	Ref.
Poly-(Au_8-DCP@Fe)	0.5 M $KHCO_3$	**-0.57**	**90 %**	This work
Au_{25} cluster	0.5 M $KHCO_3$	**-0.57**	**73.7 %**	**1**
Au_{11}	0.5 M $KHCO_3$	**-1.00**	**> 80 %**	**2**
Pd_1Au_{24}	0.1 M $KHCO_3$	**-1.00**	**100 %**	**3**
$Au_{47}Cd_2$ cluster	0.5 M $KHCO_3$	**-0.57**	**96 %**	**4**
Au_{44} cluster	0.5 M $KHCO_3$	**-0.57**	**83 %**	**4**
$Au_{24}Cd_1(PET)_{18}$ cluster	0.5 M $KHCO_3$	**-0.60**	**87.3 %**	**5**
Au_{23}	0.5 M $KHCO_3$	**-0.67**	**65 %**	**6**
$Au_{19}Cd_2$	0.5 M $KHCO_3$	**-0.67**	**95 %**	**6**
Au_{28}/CNTs	0.5 M $KHCO_3$	**-0.57**	**96.5 %**	**7**
Au_{38}	3.0 M KOH	**-0.77**	**~100 %**	**8**
Au_{144}	3.0 M KOH	**-0.77**	**~100 %**	**8**
Au_{333}	3.0 M KOH	**-0.77**	**95 %**	**8**
Au_8Ag_{55}	0.5 M $KHCO_3$	**-0.80**	**66 %**	**9**
Au_8Ag_{57}	0.5 M $KHCO_3$	**-0.80**	**61 %**	**9**
$Au_{12}Ag_{60}$	0.5 M $KHCO_3$	**-0.90**	**47 %**	**9**
Au_7/CNT	0.5 M $KHCO_3$	**-0.67**	**1.8 %**	**10**
Au_8/CNT	0.5 M $KHCO_3$	**-0.77**	**73.5 %**	**10**
Au_{44}-P	0.5 M $KHCO_3$	**-0.57**	**97 %**	**11**

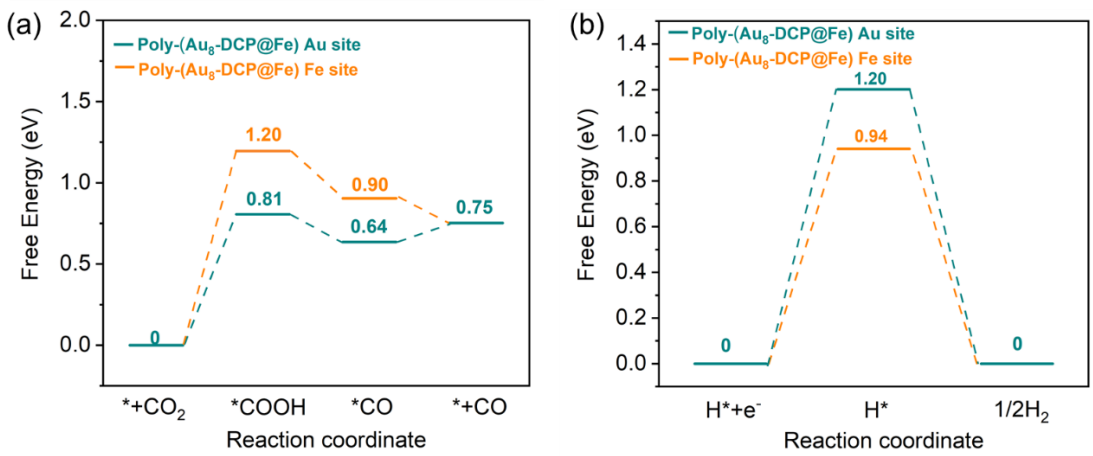

Supplementary Figure 24. The free energy diagram of the (a) CO_2RR and (b) HER on the Fe sites and Au_8 sites of Poly-(Au_8-DCP@Fe).

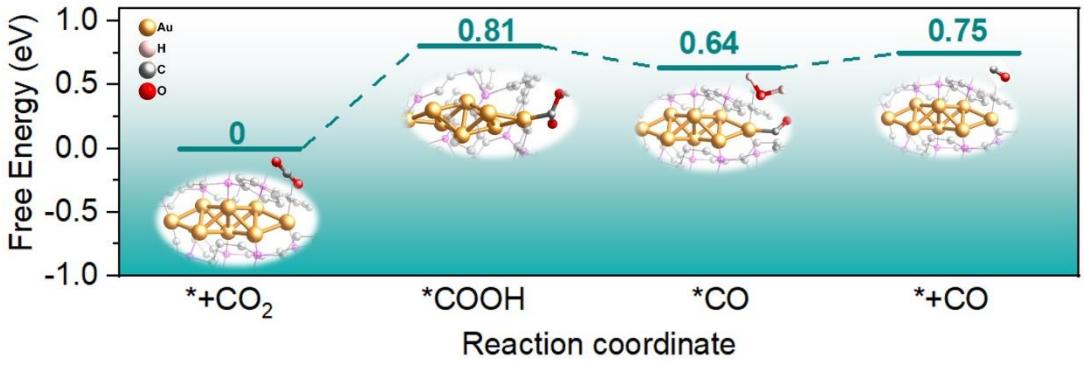

Supplementary Figure 25. Reaction paths and Free energy diagrams of CO_2 reduction to CO for Poly-(Au_8-DCP@Fe).

1 Zhao, S. et al. Influence of Atomic-Level Morphology on Catalysis: The Case of Sphere and Rod-Like Gold Nanoclusters for CO_2 Electroreduction. *ACS Catal.* **8**, 4996-5001, (2018).

2 Narouz, M. R. et al. N-heterocyclic carbene-functionalized magic-number gold nanoclusters. *Nature Chem.* **11**, 419-425, (2019).

3 Li, S. et al. Monopalladium Substitution in Gold Nanoclusters Enhances CO_2 Electroreduction Activity and Selectivity. *ACS Catal.* **10**, 12011-12016, (2020).

4 Zhuang, S. et al. Hard-Sphere Random Close-Packed $Au_{47}Cd_2(TBBT)_{31}$ Nanoclusters with a Faradaic Efficiency of Up to 96 % for Electrocatalytic CO_2 Reduction to CO. *Angew. Chem. Int. Ed.* **59**, 3073-3077, (2020).

5 Sun, Y., Liu, X., Xiao, K., Zhu, Y. & Chen, M. Active-Site Tailoring of Gold Cluster Catalysts for Electrochemical CO_2 Reduction. *ACS Catal.* **11**, 11551-11560, (2021).

6 Li, S. et al. Boosting CO_2 Electrochemical Reduction with Atomically Precise Surface Modification on Gold Nanoclusters. *Angew. Chem. Int. Ed.* **60**, 6351-6356, (2021).

7 Yuan, S. F. et al. Robust Gold Nanocluster Protected with Amidinates for Electrocatalytic CO_2 Reduction. *Angew. Chem. Int. Ed.* **60**, 14345-14349, (2021).

8 Li, S. et al. Dissecting Critical Factors for Electrochemical CO_2 Reduction on Atomically Precise Au Nanoclusters. *Angew. Chem. Int. Ed.* **61**, e202211771, (2022).

9 Hu, J. et al. Evolution of Electrocatalytic CO_2 Reduction Activity Induced by Charge Segregation in Atomically Precise AuAg Nanoclusters Based on Icosahedral M(13) Unit 3D Assembly. *Small*, e2301357, (2023).

10 Tang, L. et al. Poly-Hydride $[Au^{I}_{7}(PPh_3)_7H_5](SbF_6)_2$ cluster complex: Structure, Transformation, and Electrocatalytic CO_2 Reduction Properties. *Angew. Chem. Int. Ed.* **62**, e202300553, (2023).

11 Zhuang, S. et al. Phosphine-Triggered Structural Defects in Au(44) Homologues Boost Electrocatalytic CO_2 Reduction. *Angew. Chem. Int. Ed.*, e202306696, (2023).